2024 IEEE International Conference on Robotics and Automation (ICRA 2024)
May 13-17, 2024. Yokohama, Japan

Untethered Bimodal Robotic Fish with Tunable Bistability

Xu Chao[1,2], Imran Hameed[1,2], David Navarro-Alarcon[1], and Xingjian Jing[2*]

Abstract— **In nature, fish are excellent swimmers due to their flexible and precise control of tail, which allows them to freely transform between the smooth flapping and the motion of rapid response so that they can move with dexterity. Here, inspired by the versatile motion abilities of fish, a novel robotic fish has been developed, featuring the capability of adaptable bistability. Through tuning the bistability, the robot can acquire two locomotion modes, namely monostable and bistable modes, and it can also swim at different energy barrier that needs to be overcome to realize the bistable motion. The theoretical models are derived to facilitate the control of the robot and the understanding of its nonlinear behavior. The impact of the tunable bistability on the swimming and turning performance is investigated through extensive experiments. The study effectively demonstrates the robotic fish's capability to swiftly and efficiently navigate through mode switches, enabled by its tunable bistability. This feature is essential for underwater robots to perform tasks in intricate environments.**

I. Introduction

Good maneuverability is essential for underwater robots to accomplish tasks in unstructured and complex aquatic environments. Biomimetic methods empower robots to imitate the behaviors of animals which are proved to be superior after millions of years' natural selection [1]–[3]. In nature, fish are extraordinary swimmers for their remarkable dexterity in water [4]–[6]. They can quickly accelerate and turn to initiate a fast start and escape response [7], [8], which is crucial for their survival while avoiding predators and hunting. However, such a rapid motion is difficult to be replicated by either traditional underwater robots or the most bioinspired robotic swimmers due to the performance limitations of the actuators. Normally, rapid movements require high strain energy storage and a sudden release of a large amounts of mechanical energy [9], [10]. Researchers noticed that structures with bistability or multistability can be utilized to achieve fast response, amplify force, and enhance the energy conversion performance by leveraging the snap-through instabilities [11]–[13], and this phenomenon has extensive applications such as energy harvesting [14], [15].

Recently, the elastic instabilities have attracted tremendous interest of researchers in the field of biomimetic soft robotics, which can apparently overcome the inherent drawbacks of soft robots and enable them a further step to approach to the real applications. For example, the bistable linkages in [16] have been leveraged as the spine of terrestrial and aquatic robots to achieve high-speed and high-force locomotion. An untethered soft robot has harnessed bistable shape memory polymer muscles to amplify aquatic propulsive force [17]. And the soft swimmers constructed by hair-clip mechanisms take advantage of bistability as well to improve swimming performance [18], [19]. Despite the studies referenced above have enhanced the capability of soft robots to be applied into the real practice, they are all related to the elastic instabilities without the competence of tunability, and the snap-through movement is difficult to be controlled precisely, which is a major limitation for further performance improvement of fish robots during performing tasks. As a matter of fact, fish usually cruise smoothly in water and only exhibit the suddenly rapid movement when necessary. Such a behavior should also be endowed to robotic fish so that they can swim dexterously.

To address the challenges, we seek to leverage the tunable bistability for improving the swimming performance of a biomimetic robotic fish. Tunable bistability allows robotic fish to possess two different swimming modes including monostable mode and bistable mode, by which the robot not only can swim smoothly but also can exhibit the rapid movement. In addition, exploring the influence of different energy barrier that needs to be overcome for snap-through process of the bistable mode on the propulsion will be beneficial to high-efficient and high-speed swimming of robotic fish. And the turning performance of robotic fish can likewise be enhanced by harnessing the elastic instability. More importantly, the agile and efficient swimming of the robotic fish can be unlocked by the flexible switch between monostable and bistable modes.

This paper presents a Tunable-Bistability Fish Robot (TB-FiBot). The major contributions can be summarized as follows: (i) through combining a parallel mechanism and an elastic spine, a novel robotic fish that has the capability of tunable bistability is designed to be employed for investigation on the swimming performance improvement by strategies of tuning bistability; (ii) the theoretical models of monostable and bistable modes are developed respectively to facilitate the control of the robot and the understanding of the nonlinear behavior such as the actuation characteristics, strain energy, etc.; (iii) the influence of tunable bistability on the performances of forward swimming and turning of TB-FiBot are experimentally examined and compared. This is the first time to exploit the tunable bistability to improve the maneuverability of robotic fish, and the results of this study bring new insight into biomimetic underwater robot design.

The rest of this paper is organized as follows. Section II presents the design principle of the robotic fish in detail. In

This work was supported by the startup fund of City University of Hong Kong (9380140) and a Shenzhen-HK-Macau Scheme-C fund (9240115).

[1]Department of Mechanical Engineering, The Hong Kong Polytechnic University, Hong Kong, China
[2]Department of Mechanical Engineering, City University of Hong Kong, Hong Kong, China
*Corresponding Author: xingjing@cityu.edu.hk

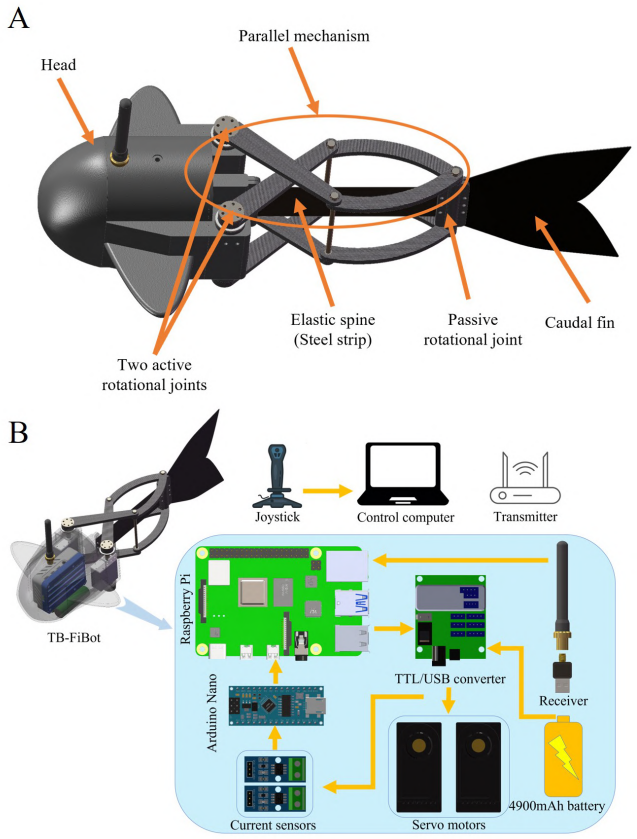

Fig. 1. TB-FiBot system overview. (A) Mechanical structure. (B) Control electronics.

section III, the theoretical models are derived and analyzed to assist the motion control of robot. The results and discussions of simulations and experiments are elaborated in section IV. Finally, the conclusions are summarized in section V.

II. Robot Design Principle

A. Mechanical Design

Fig. 1A depicts the overall mechanical structure of TB-FiBot. The robot can be separated into three parts: a head, an elastic tail, and a flexible caudal fin. The head is a waterproof housing for electronic components, and it connects with the elastic tail by two active rotational joints. The tail consists of a parallel mechanism and a spine. The spine is an elastic steel strip, which is actuated by the parallel mechanism. The parallel mechanism, namely X structure, is composed of four bars. A flexible caudal fin is connected to the tail by a passive rotational joint to supply the propulsive force. The case of head is sealed by a rubber ring, and two shafts in the active rotational joints are sealed by two rotary sealing rings. The main specifications of the robot are summarized in Table I.

B. Control System

The electronic components are illustrated in Fig. 1B. Two servo motors in the active joints are controlled by the main controller Raspberry Pi 4B+ through a TTL/USB converter and powered by a battery with the capacity of 4900 mAh.

TABLE I
Specifications of TB-FiBot

Items	Value
Robot dimensions	460 mm × 218 mm × 120 mm
Weight	1 kg
Stiffness of the elastic spine	200 Gpa
Dimensions of the elastic spine	140 mm × 0.35 mm × 50 mm

The 2.4 GHz transmitter and receiver are used for wireless remote control. The energy consumption of each motor can be estimated by the current measurement from two current sensors, which is read by the Arduino nano.

III. Modeling and Analysis

A. Inverse Kinematics

In order to achieve the flexible control of tail, the parameters of the parallel mechanism are defined as shown in Fig. 2A. And the rotational angles of two motors in the active joints can be calculated by the inverse kinematics while the trajectory of the end point E is known. The vector loop-closure equations of the parallel mechanism can be expressed as

$$\begin{cases} l_3 e^{i\varphi_5} = l_1 e^{i\varphi_1} + l_2 e^{i\varphi_4} \\ l_4 e^{i\varphi_6} = l_1 e^{i\varphi_2} + l_2 e^{i\varphi_3} \end{cases} \tag{1}$$

where l_1, l_2, l_3, and l_4 are the lengths of AB, CD, BE, and CE respectively, φ_1 to φ_5 are the rotational angles (Fig. 2A). The above equations can be simplified and then we can get the following equations.

$$\begin{cases} 2l_1 l_3 \cos(\varphi_1 - \varphi_5) + l_2^2 - l_1^2 - l_3^2 = 0 \\ 2l_1 l_4 \cos(\varphi_2 - \varphi_6) + l_2^2 - l_1^2 - l_4^2 = 0 \end{cases} \tag{2}$$

By solving the above two equations, φ_1 and φ_2 can be expressed as

$$\begin{cases} \varphi_1 = \arccos\left(\dfrac{l_3^2 + l_1^2 - l_2^2}{2l_1 l_3}\right) + \varphi_5 \\ \varphi_2 = \arccos\left(\dfrac{l_4^2 + l_1^2 - l_2^2}{2l_1 l_4}\right) + \varphi_6 \end{cases} \tag{3}$$

B. Monostable Mode

For the monostable mode, the trajectory of the end point E of the parallel mechanism can be obtained by assuming the curve of the elastic spine is a part of a circle as shown in Figure 2(B) and is calculated by the following equations.

$$\begin{cases} x_E^0 = d_1 + r_c \sin\alpha_c + \dfrac{d_2}{2}\cos\alpha_c \\ y_E^0 = r_c(1 - \cos\alpha_c) + \dfrac{d_2}{2}\sin\alpha_c \end{cases} \tag{4}$$

where $r_c = L_s/\alpha_c$, $\alpha_c = \sin(2\pi f t + b)$, a, f, and b are amplitude, frequency, and bias angle, respectively.

Then the force-displacement relation of the elastic spine can be derived by the chained beam constraint model (CBCM) [20].

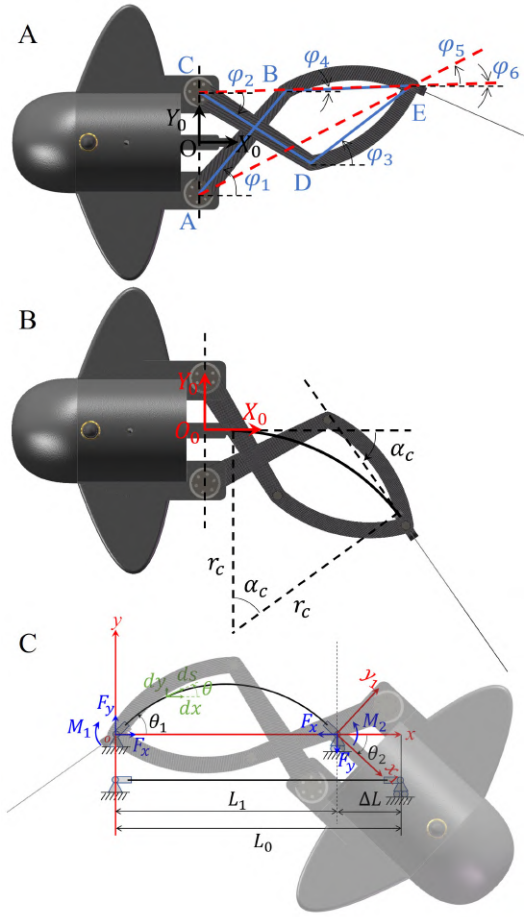

Fig. 2. Schemas of tail's parameters. (A) kinematics of the parallel mechanism. (B) Monostable mode. (C) Bistable mode

$$\begin{cases} \begin{bmatrix} f_{yi} \\ m_i \end{bmatrix} = Q_1 \begin{bmatrix} y_i \\ \theta_i \end{bmatrix} + f_{xi} Q_2 \begin{bmatrix} y_i \\ \theta_i \end{bmatrix} + f_{xi}^2 Q_3 \begin{bmatrix} y_i \\ \theta_i \end{bmatrix} \\ x_i = \dfrac{t^2 f_{xi}}{12} - \dfrac{1}{2} \begin{bmatrix} y_i & \theta_i \end{bmatrix} Q_2 \begin{bmatrix} y_i \\ \theta_i \end{bmatrix} - f_{xi} \begin{bmatrix} y_i & \theta_i \end{bmatrix} Q_3 \begin{bmatrix} y_i \\ \theta_i \end{bmatrix} \end{cases} \tag{5}$$

And the strain energy stored in the deflected elastic spine can be calculated as follows.

$$v_i = \frac{1}{2}\frac{t^2 f_{xi}^2}{12} + \frac{1}{2} \begin{bmatrix} y_i & \theta_i \end{bmatrix} Q_1 \begin{bmatrix} y_i \\ \theta_i \end{bmatrix} - \frac{1}{2} f_{xi}^2 \begin{bmatrix} y_i & \theta_i \end{bmatrix} Q_3 \begin{bmatrix} y_i \\ \theta_i \end{bmatrix} \tag{6}$$

where $t = nT/L_0$, $x_i = nX_i/L_0$, $y_i = nY_i/L_0$, $f_xi = F_{xi}L_0^2/(n^2EI)$, $f_{yi} = F_{yi}L_0^2/(n^2EI)$, $m_i = M_iL/(nEI)$, $Q_1 = [12, -6; -6, 4]$, $Q_2 = [6/5, -1/10; -1/10, 2/15]$, $Q_3 = [-1/700, 1/1400; 1/1400, -11/6300]$.

For two adjacent segments, the following equations can be derived by the moment relations.

$$M_{i-1} = F_{xi}Y_i + F_{yi}\left(\frac{L_0}{n} + X_i\right) + M_i \tag{7}$$

where M_i, F_{xi}, and F_{yi} are the moment and forces exerted on the ith segment by the $(i+1)$th segment, respectively.

C. Bistable Mode

The bistable mode can be achieved by compressing the elastic spine. When the end point E of the parallel mechanism is assumed to be fixed and the head is assumed to rotate around a fixed point, the elastic can be regarded as a pinned-pinned buckled beam, and the bistable mode can be realized by applying moment on the head as shown in Fig. 2C.

To acquire the trajectory of the end point E of the parallel mechanism, the position and rotation transformation between the frame oxy and $o_1x_1y_1$ can be calculated by

$$P_E = P_1 + R_1 P_E^1 \tag{8}$$

where $R_1 = [\cos\theta_2, -\sin\theta_2; \sin\theta_2, \cos\theta_2]$, $P_1 = [L_1, 0]^T$, and $P_E = [0, 0]^T$.

To get the parameters of the control and understand the nonlinear behavior of the elastic spine during the bistable mode, we use an analytical model derived based on Euler-Bernoulli beam theory [21].

The bending moment of the elastic spine can be expressed as

$$M(s) = -F_x y(s) + F_y x(s) + M_1 \tag{9}$$

where s is the arc length of the elastic spine. Through the linearization of $x(s)$ $(x(s) \approx (L_1/L_0)s)$ and applying the boundaries conditions $y(s=0) = 0$, $y(s=L_0) = 0$, $y''(s=0) = 0$, the above equation can be solved as

$$y(s) = A\left(\sin\left(kL_0\frac{s}{L_0}\right) - \sin(kL_0)\frac{s}{L_0}\right) \tag{10}$$

where $k = \sqrt{\frac{F_x}{EI}}$.

Then the following relations can be obtained.

$$\begin{cases} E_s = \dfrac{1}{4}\dfrac{EI}{L_0}\left(\dfrac{A}{L_0}\right)^2 (kL_0)^3 \left(kL_0 - \dfrac{\sin(2kL_0)}{2}\right) \\ M_2 = -\dfrac{EI}{L_0}\dfrac{A}{L_0}(kL_0)^2\sin(kL_0) \\ \theta_1 = \dfrac{A}{L_0}(kL_0 - \sin(kL_0)) \\ \theta_2 = \dfrac{A}{L_0}(kL_0\cos(kL_0) - \sin(kL_0)) \end{cases} \tag{11}$$

IV. Results and Discussions

A. Tunable Bistability

Based on the models in the last section, different swimming modes and turning modes can be realized by trajectory control of the end point E of the elastic spine. Figs. 3A and B show the deformed shape and the strain energy of the elastic spine when following the trajectory of point E of monostable mode. During each swing cycle of tail, the elastic spine always recovers to the undeformed state. Thus, only one valley can be seen from the curve of its strain energy where the value is zero. Fig. 3C demonstrates the deformed shape of the elastic spine for the bistable swimming mode. In this mode, the elastic spine is in the compressed state all

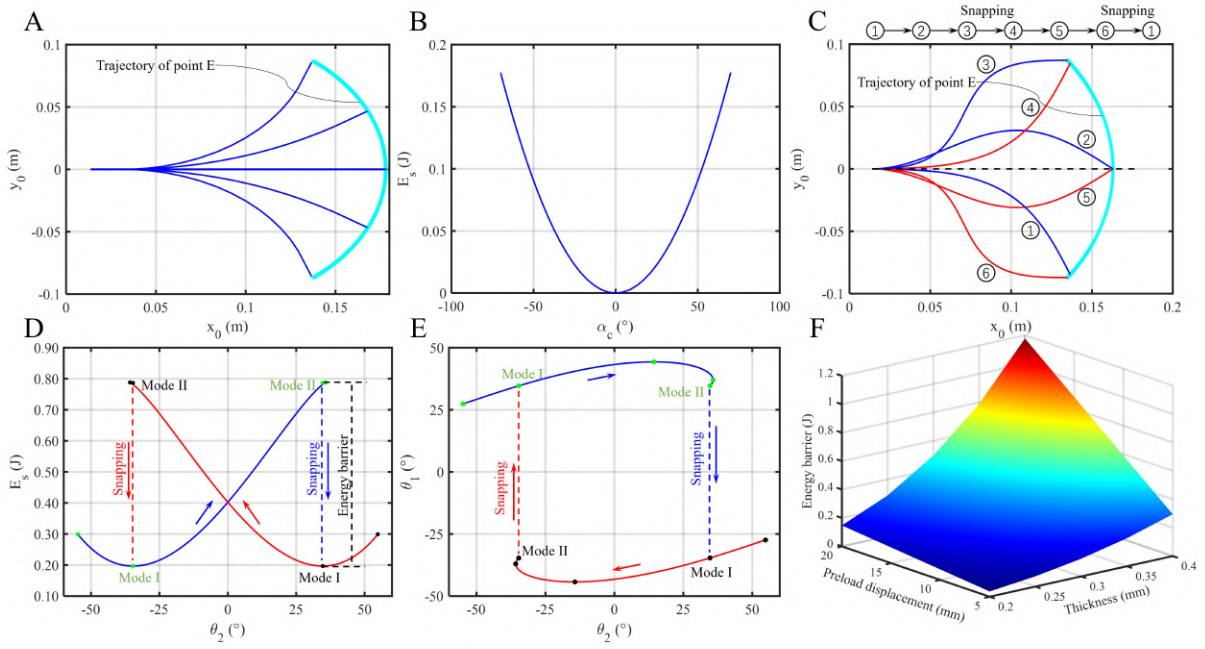

Fig. 3. (A) Deformed shape of elastic spine for monostable mode. (B) Strain energy of elastic spine for monostable mode. (C) Deformed shape of elastic spine for bistable mode. (D) Strain energy of elastic spine for bistable mode. (E) Angles relation of bistable mode. (F) Energy barrier versus preload displacement and thickness of elastic spine for bistable mode.

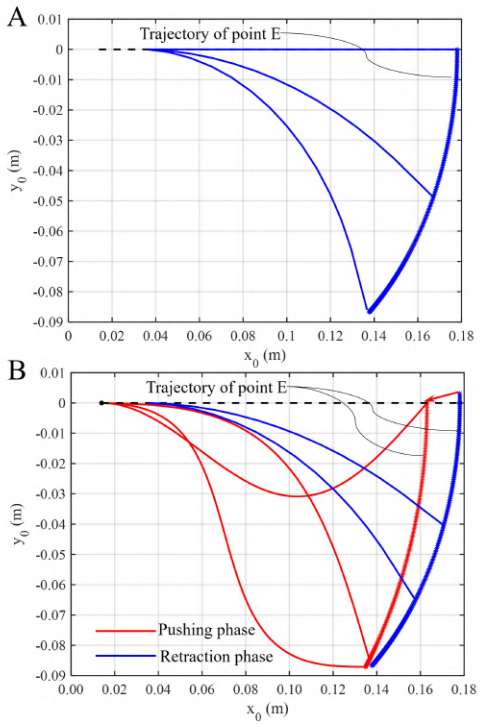

Fig. 4. (A) Monostable turning mode. (B) Bistable turning mode.

the time. And there is the motion of snapping which can be observed from the strain energy and the angles relation as shown in Figs. 3D and E, respectively. Different energy barriers that need to be overcome for achieving snapping motion can be realized by different preload compressions and different thicknesses of the elastic spine as shown in Fig. 3F.

In Fig. 4, the realization of two different turning modes is illustrated. Fig. 4A shows the monostable turning mode, namely C-shape turning. Through combining the trajectories of point E of monostable mode and bistable mode, the snapping motion can be utilized for the turning as shown in Fig. 4B. For the pushing phase, point E follows the trajectory of bistable mode, and for the retraction phase, point E moves along the trajectory of the monostable mode.

The above results of the modeling facilitate us to better understand the nonlinear behaviors of the elastic spine during its movement and to obtain the control inputs of two active rotational joints for different flapping modes so that the precise control of the tail and the switching between different swimming modes can be easily achieved.

B. Swimming Performance

To evaluate the straight-line swimming performance of TB-FiBot, the velocity and the cost of transport at different frequencies of 0.5-3 Hz and different amplitudes of 7, 8 and 9 cm is compared. The cost of transport (CoT) denotes the swimming efficiency, which is defined as energy consumption per unit distance [22] and can be calculated by the following equation.

$$\mathrm{CoT} = \frac{P}{V} \tag{12}$$

where P is the power consumption and V is the average swimming velocity. A 2-joint robotic fish with series structure as shown in Fig. 5 is also in the comparison for the

Fig. 5. Compared 2-joint robotic fish.

better evaluation. The size of the 2-joint robotic fish is 460 mm × 80 mm × 80 mm.

According to the experimental results shown in Fig. 6, TB-FiBot can achieve the fastest speed through the bistable swimming mode at all test cases, especially at low frequencies, which is almost twice the speed of the monostable swimming mode. However, the propulsive efficiency of the bistable swimming mode is much lower than that of the monostable swimming mode at low frequencies. At high frequencies, the energy consumption of the bistable mode is close to but slightly higher than that of the monostable mode. Therefore, the robot can choose either fast swimming or energy-saving swimming through the motion modes switching for different mission purposes. The velocity of the compared 2-joint robotic fish is close to the velocity of the monostable mode, but its energy consumption is much higher than both modes of TB-FiBot. The maximum velocity of TB-FiBot is around 1.35 BL/s (0.62 m/s) at the frequency of 3 Hz and the amplitude of 9 cm. And the propulsive efficiency under the maximum speed is about 24 J/m. The snapshots of straight swimming at the frequency of 1 Hz and the amplitude of 9 cm for the bistable mode and the monostable mode are demonstrated in Fig. 7.

C. Turning Performance

The influence of the tunable bistability on the turning performance is also examined. The angular velocity and the turning efficiencies of two turning modes of TB-Fibot and 2-joint robotic fish under different frequencies of 0.5 to 3 Hz and different amplitudes of 8 and 9 cm is evaluated. The cost of turning (CoTu) is used to estimate the turning efficiency, which is defined in the style of the cost of transport (CoT) as

$$\text{CoTu} = \frac{P}{\omega} \tag{13}$$

where ω is the average angular velocity.

The experimental results of the turning performance are illustrated in Fig. 8. It is obvious to see that the angular speed can be improved dramatically by the bistable turning mode (Figs. 8A and B). And at low frequencies as well, the angular velocity of bistable turning mode is much higher than that of the monostable turning mode, which is enlarged by two to three times. When the frequency is high or ultra-low, the bistable turning mode performs better in turning efficiency

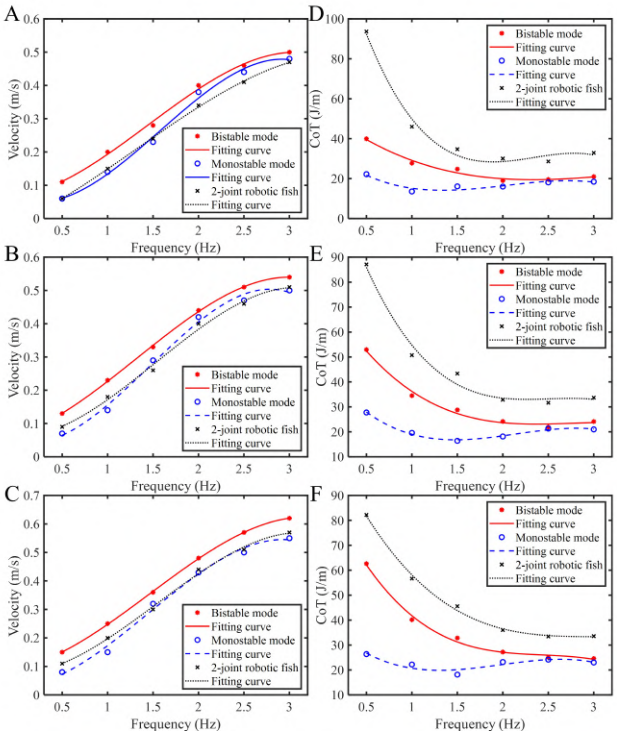

Fig. 6. (A) to (C) Swimming velocity. (D) to (F) Cost of transport. Amplitude: 7 cm (top), 8 cm (middle), 9 cm (bottom).

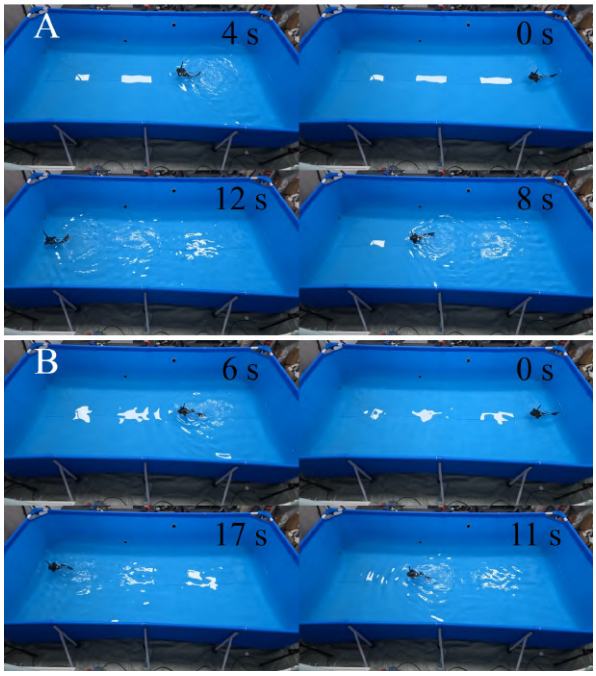

Fig. 7. Snapshots of swimming at frequency of 1 Hz and amplitude of 9 cm: (A) Bistable mode. (B) Monostable mode.

(Figs. 8C and D). But in the range of frequency from 1 to 2 Hz, the turning efficiency of monostable mode is much higher than that of the bistable turning mode. For the turning performance of 2-joint robotic fish, its angular velocity is higher than the monostable turning mode but lower than the

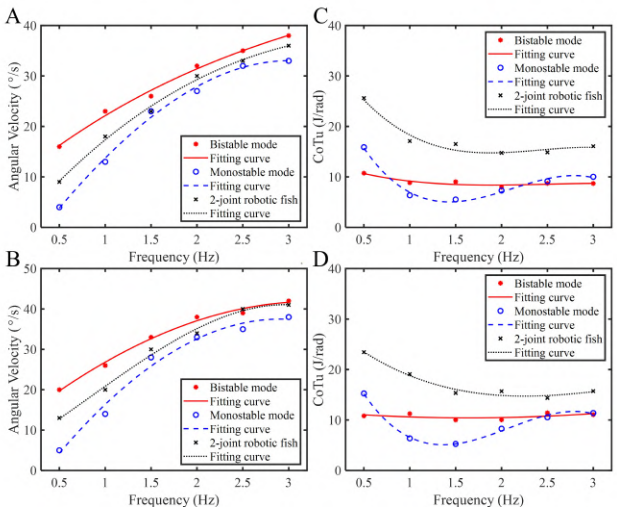

Fig. 8. (A) and (B) Angular velocity. (C) and (D) Cost of turning. Amplitude: 8 cm (top), 9 cm (bottom).

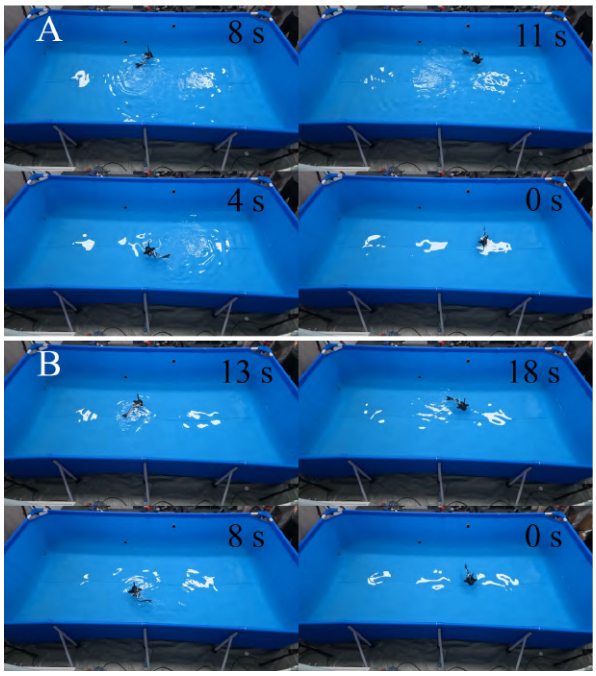

Fig. 9. Snapshots of turning at frequency of 1 Hz and amplitude of 9 cm: (A) Bistable mode. (B) Monostable mode.

bistable turning mode. And its energy consumption is much greater than that of both turning modes of TB-Fibot. The maximum angular velocity of TB-Fibot is about 42 degrees per second with the CoTu of 11 J/rad when the frequency is 3 Hz and the amplitude is 9 cm. Fig. 9 shows the snapshots of turning at the frequency of 1 Hz and the amplitude of 9 cm for the bistable and the monostable modes.

D. Comparison with Other Robots

The comparisons between TB-FiBot in this article with some robotic fish from the literature are summarized in Table II. WE-Rofi [5] is a wire-driven robotic fish, which is also

TABLE II
COMPARISONS WITH OTHER PLATFORMS

Platform	Max velocity (m/s, BL/s)	CoT (J/m)	Frequency (Hz)
WE-Rofi [5]	0.58, 1.04	24	5
RobotShark [5]	0.43, 0.66	62	2
HasorTuna [23]	0.36, 0.63	58	3.5
robotic fish [19]	0.44, 2.03	-	-
ours	0.62, 1.35	24	3

driven by two servos and incorporates elastic steel strip in its tail structure. Robotshark [5] is a multi-joint robotic fish with series structure, and in its experiments, only two servos in two joints are used as well. HasorTuna [23] is a hydraulic soft robotic Tuna, which uses two servos to actuate the piston, and the main feature is that its stiffness of caudal peduncle can be tuned to improve its swimming performance. Robotic fish in [19] achieves fast speed by a bistable mechanism, namely hair clip mechanism (HCM).

From the results of comparisons, it can be observed that our robot is the fastest, and the cost of transport of TB-FiBot at the maximum speed is much lower than RobotShark and HasorTuna. Although the performance of WE-Rofi is close to our robot, its body length is larger and it needs much higher frequency to achieve fast speed. Compared to robotic fish in [19] which can only perform snapping motion, TB-FiBot shows higher motion flexibility and better maneuverability. The comparisons further demonstrate good swimming performance of TB-FiBot with respect to high speed and high energy efficiency because of tunable bistability.

V. CONCLUSION AND FUTURE WORK

In this work, we present a novel robotic fish with tunable bistability. Through the trajectory control of end point of the elastic spine, different swimming and turning modes can be realized, which allows the robotic fish to adapt to different usage scenarios and environments. Based on the above results and discussions, the following conclusions can be drawn.

1) The bistable swimming mode enables the robotic fish to swim fast. Especially at low frequencies, the velocity can be dramatically improved.
2) The monostable swimming mode is the most energy efficient. At low frequencies, its energy consumption is much lower than that of the bistable swimming mode.
3) The turning performance of the robotic fish can be enhanced by the combination of the trajectory of the bistable mode and the monostable mode. The angular velocity can be increased remarkably at low frequencies through the bistable turning mode.

In future work, we will further explore the performance improvement of the robotic fish with tunable bistability through the stiffness optimization of the elastic spine and the caudal fin. And the active controlled pectoral fins will be added to realize flexible swimming of the robot in three-dimensional underwater space.

REFERENCES

[1] Y. Wang, X. Yang, Y. Chen, D. K. Wainwright, C. P. Kenaley, Z. Gong, Z. Liu, H. Liu, J. Guan, T. Wang, *et al.*, "A biorobotic adhesive disc for underwater hitchhiking inspired by the remora suckerfish," *Science Robotics*, vol. 2, no. 10, p. eaan8072, 2017.

[2] Z. Li, X. Chao, I. Hameed, J. Li, W. Zhao, and X. Jing, "Biomimetic omnidirectional multi-tail underwater robot," *Mechanical Systems and Signal Processing*, vol. 173, p. 109056, 2022.

[3] F. Berlinger, M. Duduta, H. Gloria, D. Clarke, R. Nagpal, and R. Wood, "A modular dielectric elastomer actuator to drive miniature autonomous underwater vehicles," in *2018 IEEE International Conference on Robotics and Automation (ICRA)*. IEEE, 2018, pp. 3429–3435.

[4] M. Sfakiotakis, D. M. Lane, and J. B. C. Davies, "Review of fish swimming modes for aquatic locomotion," *IEEE Journal of oceanic engineering*, vol. 24, no. 2, pp. 237–252, 1999.

[5] X. Liao, C. Zhou, Q. Zou, J. Wang, and B. Lu, "Dynamic modeling and performance analysis for a wire-driven elastic robotic fish," *IEEE Robotics and Automation Letters*, vol. 7, no. 4, pp. 11 174–11 181, 2022.

[6] Q. Zhong, J. Zhu, F. E. Fish, S. J. Kerr, A. Downs, H. Bart-Smith, and D. Quinn, "Tunable stiffness enables fast and efficient swimming in fish-like robots," *Science Robotics*, vol. 6, no. 57, p. eabe4088, 2021.

[7] A. D. Marchese, C. D. Onal, and D. Rus, "Autonomous soft robotic fish capable of escape maneuvers using fluidic elastomer actuators," *Soft robotics*, vol. 1, no. 1, pp. 75–87, 2014.

[8] I. Borazjani, F. Sotiropoulos, E. D. Tytell, and G. V. Lauder, "Hydrodynamics of the bluegill sunfish c-start escape response: three-dimensional simulations and comparison with experimental data," *Journal of Experimental Biology*, vol. 215, no. 4, pp. 671–684, 2012.

[9] J.-S. Koh, E. Yang, G.-P. Jung, S.-P. Jung, J. H. Son, S.-I. Lee, P. G. Jablonski, R. J. Wood, H.-Y. Kim, and K.-J. Cho, "Jumping on water: Surface tension–dominated jumping of water striders and robotic insects," *Science*, vol. 349, no. 6247, pp. 517–521, 2015.

[10] M. Noh, S.-W. Kim, S. An, J.-S. Koh, and K.-J. Cho, "Flea-inspired catapult mechanism for miniature jumping robots," *IEEE transactions on robotics*, vol. 28, no. 5, pp. 1007–1018, 2012.

[11] S. Nishikawa, Y. Arai, R. Niiyama, and Y. Kuniyoshi, "Coordinated use of structure-integrated bistable actuation modules for agile locomotion," *IEEE Robotics and Automation Letters*, vol. 3, no. 2, pp. 1018–1024, 2018.

[12] J. T. Overvelde, T. Kloek, J. J. D'haen, and K. Bertoldi, "Amplifying the response of soft actuators by harnessing snap-through instabilities," *Proceedings of the National Academy of Sciences*, vol. 112, no. 35, pp. 10 863–10 868, 2015.

[13] Y. Cao, M. Derakhshani, Y. Fang, G. Huang, and C. Cao, "Bistable structures for advanced functional systems," *Advanced Functional Materials*, vol. 31, no. 45, p. 2106231, 2021.

[14] A. Arrieta, P. Hagedorn, A. Erturk, and D. J. Inman, "A piezoelectric bistable plate for nonlinear broadband energy harvesting," *Applied Physics Letters*, vol. 97, no. 10, 2010.

[15] F. Cottone, L. Gammaitoni, H. Vocca, M. Ferrari, and V. Ferrari, "Piezoelectric buckled beams for random vibration energy harvesting," *Smart materials and structures*, vol. 21, no. 3, p. 035021, 2012.

[16] Y. Tang, Y. Chi, J. Sun, T.-H. Huang, O. H. Maghsoudi, A. Spence, J. Zhao, H. Su, and J. Yin, "Leveraging elastic instabilities for amplified performance: Spine-inspired high-speed and high-force soft robots," *Science advances*, vol. 6, no. 19, p. eaaz6912, 2020.

[17] T. Chen, O. R. Bilal, K. Shea, and C. Daraio, "Harnessing bistability for directional propulsion of soft, untethered robots," *Proceedings of the National Academy of Sciences*, vol. 115, no. 22, pp. 5698–5702, 2018.

[18] Y. Chi, Y. Hong, Y. Zhao, Y. Li, and J. Yin, "Snapping for high-speed and high-efficient butterfly stroke–like soft swimmer," *Science Advances*, vol. 8, no. 46, p. eadd3788, 2022.

[19] Z. Xiong, Y. Su, and H. Lipson, "Fast untethered soft robotic crawler with elastic instability," in *2023 IEEE International Conference on Robotics and Automation (ICRA)*. IEEE, 2023, pp. 2606–2612.

[20] F. Ma and G. Chen, "Modeling large planar deflections of flexible beams in compliant mechanisms using chained beam-constraint-model," *Journal of Mechanisms and Robotics*, vol. 8, no. 2, p. 021018, 2016.

[21] L. Tissot-Daguette, H. Schneegans, E. Thalmann, and S. Henein, "Analytical modeling and experimental validation of rotationally actuated pinned–pinned and fixed–pinned buckled beam bistable mechanisms," *Mechanism and Machine Theory*, vol. 174, p. 104874, 2022.

[22] J. Zhu, C. White, D. K. Wainwright, V. Di Santo, G. V. Lauder, and H. Bart-Smith, "Tuna robotics: A high-frequency experimental platform exploring the performance space of swimming fishes," *Science Robotics*, vol. 4, no. 34, p. eaax4615, 2019.

[23] S. Liu, C. Liu, Y. Liang, L. Ren, and L. Ren, "Tunable stiffness caudal peduncle leads to higher swimming speed without extra energy," *IEEE Robotics and Automation Letters*, 2023.